PCCP

Accepted Manuscript

ROYAL SOCIETY OF CHEMISTRY

www.rsc.org/pccp

TOC Entry

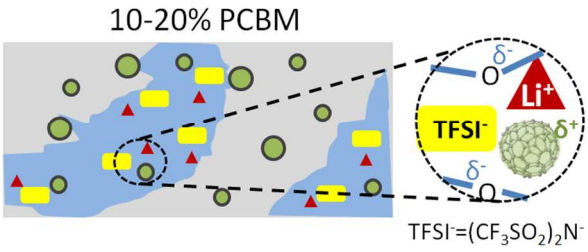

We report a 6-fold ion conductivity enhancement in PEO/LiTFSI –based solid electrolytes upon the addition of fullerene derivatives.

Nanostructure Enhanced Ionic Transport in Fullerene Reinforced Solid Polymer Electrolytes

Che-Nan Sun, Thomas A. Zawodzinski Jr.,Wyatt E. Tenhaeff, Fei Ren, Jong Kahk Keum, Sheng Bi, Dawen Li, Suk-Kyun Ahn, Kunlun Hong, Adam J. Rondinone, Jan-Michael Y. Carrillo, Changwoo Do, Bobby G. Sumpter, Jihua Chen*

Dr. C.N. Sun, Prof. T. A. Zawodzinski,
Materials Science & Technology Division, Oak Ridge National Laboratory P.O. Box 2008. Oak Ridge, TN, USA
Prof. T. A. Zawodzinski
Department of Chemical and Biomolecular Engineering, University of Tennessee, Knoxville, TN 37996, USA
Prof. W. E. Tenhaeff
Department of Chemical Engineering, University of Rochester, Rochester, NY 14627 USA
Prof. F. Ren
Department of Mechanical Engineering, Temple University, Philadelphia, PA 19122 USA
Dr. J.K. Keum, Dr. C. Do
Neutron Scattering Science Division, Oak Ridge National Laboratory, Oak Ridge, TN 37831, USA
S. Bi, Prof. D. Li
Department of Electrical and Computer Engineering, Center for Materials Information Technology, University of Alabama, Tuscaloosa, AL 35487, USA
Dr. B. G. Sumpter, Dr. J.-M.Y. Carrillo
Computer Science and Mathematics Division, Oak Ridge National Laboratory P.O. Box 2008. Oak Ridge, TN, USA
Dr. B. G. Sumpter, Dr. S. K. Ahn, Dr. K. Hong, Dr. A. J. Rondinone, Dr. J.-M.Y. Carrillo, Dr. J. Chen
Center for Nanophase Materials Sciences, Oak Ridge National Laboratory, Oak Ridge, TN 37831, USA

Corresponding author: Dr. Jihua Chen, chenj1@ornl.gov

Abstract

Solid polymer electrolytes, such as polyethylene oxide (PEO) based systems, have the potential to replace liquid electrolytes in secondary lithium batteries with flexible, safe, and mechanically robust designs. Previously reported PEO nanocomposite electrolytes routinely use metal oxide nanoparticles that are often 5-10 nm in diameter or larger. The mechanism of those oxideparticle-based polymer nanocomposite electrolytes is under debate and the ion transport performance of these systems is still to be improved. Herein we report a 6-fold ion conductivity enhancement in PEO/ lithium bis(trifluoromethanesulfonyl) imide (LiTFSI) –based solid electrolytes upon the addition of fullerene derivatives. The observed conductivity improvement correlates with nanometer-scale fullerene crystallite formation, reduced crystallinities of both $(PEO)_6$:LiTFSI phase and pure PEO, as well as significantly larger PEO free volume. This improved performance is further interpreted by enhanced decoupling between ion transport and polymer segmental motion, as well as optimized permittivity and conductivity in bulk and grain boundaries. This study suggests that nanoparticle induced morphological changes, in a system with fullerene nanoparticles and no Lewis acidic sites, play critical roles in their ion conductivity enhancement. The marriage of fullerene derivatives and solid polymer electrolytes opens up significant opportunities in designing next-generation solid polymer electrolytes with improved performance.

Solid polymer electrolytes attract significant scientific attentions because of their excellent potentials in a wide range of energy storage and energy harvest applications such as lithium batteries, high dielectric constant thin film capacitors, solid-state capacitors, supercapacitors, as well as solid-state photochemical solar cells and dye sensitized solar cells.[1-11] Solid state block copolymer electrolytes[5,7] and metal-oxide nanoparticle based polymer nanocomosites[1-4, 12] are two examples of novel solid polymer electrolytes. Block copolymer electrolytes take advantages of bottom-up self assembly as well as covalent linking of an insulating polymer block and an ion-conducting block. Metal-oxide nanoparticle based polymer nanocomposites, on the other hand, heavily rely on the geometry, size, size distribution, aggregation, and surface chemistry of metal oxide nanoparticles as well as their matrix-particle interactions. Both block copolymer electrolytes and metal-oxide/polymer nanocomposite electrolytes have been explored extensively, with their performance reaching plateau at optimized block copolymer composition or ideal metal-oxide loading. Oxide nanoparticles with individual particles sizes of 5 nm or larger were often used in previously reported nanocomposite electrolytes (typically at an optimal concentration of ~10wt%).[1-3, 13-18] The underlying mechanisms for ion conductivity enhancement in polymer nanocomposite electrolytes are still under debate. The interactions between lewis acidic sites on nanoparticle surfaces and matrix were described as a main mechanism in some studies, [1, 19] while there was evidence suggesting that nanoparticle-induced changes in polymer-matrix segmental dynamics, rotation, or crystallization suppression make dominating contributions. [4, 13, 20] These conclusions are further complicated by oxide nanoparticle aggregation and the different polymer-salt systems studied. An accurate correlation between

nanostructure and ion transport is challenging and elusive in these nanocomposite electrolyte systems.

Herein we introduce fullerene based polymer nanocomposite electrolytes as a new class of solid polymer electrolytes, and report for the first time a study on nanostructures and properties of fullerene-based solid polymer electrolytes. There are several important aspects of the fullerene-based solid state electrolytes that make them highly attractive as compared to conventional nanocomposite electrolytes: (1) The functionalized fullerenes are monodisperse, solution-processible, molecular nanoparticles, which makes it much easier to study structure-property correlations in nanocomposite electrolyte systems. Here we used a benchmark fullerene derivative $C_{72}H_{14}O_2$, known as phenyl-C_{61}-butyric acid methyl ester (PCBM), which has a molecular weight of 910.88 Da. For an oxide-particle-based composite electrolyte, the nanostructural details of polymer-nanoparticle assembly and their correlation with ion transport are scarce, partly because of the polydispersity and insolubility of oxide nanoparticles. Other factors such as inadequate solid-state mixing, particle aggregation, non-uniform dispersion, surface functionality and topographical features can further complicate these studies.
(2) Fullerenes allow a high percentage (>40wt%) of incorporation into polymer matrix, as shown in high-performance organic solar cell systems,[21] while conventional oxide nanoparticle based electrolytes have a typical nanoparticle loading of 10wt%.[1] If the comparison is made on a volumetric percentage, the differences will be even larger, considering that the reported PCBM density is typically 1.3-1.5 g/cm^3,[22-23] which is much lower than those of metal oxide nanoparticles (for example, Al_2O_3 has a density of 4 g/cm^3).[24] Fullerene derivatives such as PCBM are well known as n-type semiconductors, and thus will not contribute significantly to

leakage current of the electrolyte systems.[21] The potentially higher additive loading can provide important opportunities in further tuning structure and properties of composite electrolytes. (3)The use of fullerenes provides an unprecedentedly small additive size (0.7 nm) and well-defined surface chemistry. The geometrical dimensions of nanoparticle additives, along with their surface functionality and surface topography, were shown to have a significant impact on the local structure and ion transport of the resultant composite electrolyte systems. [14, 25]

In this work, anionically polymerized polyethylene oxide (PEO) with a number average molecular weight (Mn) of 270k and narrow polydispersity (PDI=1.1) is used as a model polymer matrix, in an effort to minimize the effects from polymer molecular weight and polydispersity. Polydispersity is well known to have a profound impact on and thus largely complicate any nanostructure-performance correlations. Polymer molecular weight also has a critical role on various aspects of the resultant electrolytes, including mechanical properties and ion conductivities. In particular, the effect of molecular weight (M) on ion conductivity (σ) of polymer electrolytes generally follows the expression of $\sigma = \sigma_0 + K/M$, where σ_0 stands for ion transport contribution from segmental motions, K is a constant, and the K/M component represents the friction contribution from coupled polymer chains and coordinated ions in the Rouse model.[6,7] Lithium bis(trifluoromethanesulfonyl) imide (LiTFSI) salt is chosen as a model salt because of its wide adoption in solid electrolyte systems and well explored phase diagram. [1-11] Using this model system with LiTFSI and large-Mn, narrow-polydispersity PEO, it is demonstrated that there is a largely enhanced ion transport (up to 600%, at temperatures less than 50^{o}C) in PEO/ LiTFSI electrolytes upon the addition of PCBM. This accompanies nano-cluster formation with systematically varied PCBM crystallite sizes, reduced PEO and $(PEO)_6$:LiTFSI

crystallinity, improved PEO dispersion and free volume, and up-to 3 fold reduction in elastic modulus and hardness. This ion transport enhancement is further attributed to permittivity and conductivity optimization at grain boundaries and in bulk as well as enhanced decoupling of ion transport from polymer segmental motions, based on equivalent circuit modelling and temperature-dependent conductivity analysis.

Figure 1a shows the temperature dependence of ionic conductivity for PEO/LiTFSI blends (with a [O:Li] ratio of 10:1) as a function of PCBM concentration (from 0 to 40wt%). The blend with 20wt% PCBM consistently exhibits the highest ionic conductivity among all systems up to 65-70^{o}C. For example, at 50^{o}C, the pristine PEO/LiTFSI has a conductivity of 3.5±0.2 $\times10^{-5}$ S/cm, while the conductivities for 10%, 20%, and 40% PCBM are respectively 1.0±0.1 $\times10^{-4}$ S/cm, 1.6±0.1 $\times10^{-4}$ S/cm, and 8.5±0.4 $\times10^{-5}$ S/cm. In the higher temperature regions (>70^{o}C), the measured conductivities do not vary significantly as the PCBM loading increases from 0 to 20%. For example, at 90^{o}C, the pristine PEO/LiTFSI has a conductivity of 6.9±0.3 $\times10^{-4}$ S/cm, while the conductivities for 10%, 20%, and 40% PCBM are 7.5±0.4 $\times10^{-4}$ S/cm, 6.7±0.3 $\times10^{-4}$ S/cm, and 3.1±0.2 $\times10^{-4}$ S/cm, respectively.

Differential scanning calorimetry results in Figure 1b show that, in the first cooling cycle (top data set), the samples with 0 and 10wt% PCBM had a distinctive PEO crystallization peak below 40^{o}C (28^{o}C for pristine PEO/LiTFSi and 18^{o}C for the blend with 10wt% PCBM),[26-29] while the crystallization in other samples was largely suppressed with higher PCBM loadings of 20-40wt%. In the second heating cycle (bottom data set in Figure 1b), again, the PEO melting temperature T_m (between 25 and 65 ^{o}C) was highly dependent on PCBM concentration, with the

peak in the samples with 0-10wt% PCBM much larger than the rest. The T_m of samples with 0-40wt% PCBM is 54 °C, 44 °C, 41 °C, and 36 °C, respectively. The dimensions of lamellar crystals of semicrystalline polymers such as PEO are important in determining the melting points of such polymers (T_m), often interpreted with the Gibbs-Thomson relationships: [30-31]

$$\frac{T_m(D)}{T_m(\infty)} = 1 - \frac{2\gamma V}{HD} \qquad (1)$$

where D denotes the thickness of a polymeric, lamellar crystal, V and H are molar volume and melting enthalpy of the crystal, and γ is the interfacial energy of the lamellar crystal and its surrounding environment. If one assumes that the thermodynamic equilibrium melting point of a perfect polymer crystal of infinite dimension $T_m(\infty)$ is constant along with V, H and γ, melting temperature of a lamellar crystal $T_m(D)$ will increase with the lamellar crystal thickness D. Based on this simplification, our results on PCBM concentration dependent melting point changes can be explained by decreased PEO crystal dimensions as the PCBM loading increases from 0 to 40wt%.

Glass transition temperature (T_g) in the first cooling and second heating cycles was plotted as a function of PCBM loading in Figure 1c, consistently showing a minimal T_g in the blend with 20wt% PCBM. Based on a theory proposed by Flory and Fox,[32] the free volume (or volume of holes between polymer segments in volume fraction) v_f is related to temperature (T) and molecular weight (M), and T_g is free volume dependent, according to the following expressions:

$$v_f = A + BT + C/M, \qquad (2)$$

$$T_g = T_g^{\infty} - \Psi(v_f)/M, \qquad (3)$$

where *A, B, C* are constants, T_g^{∞} is the maximum glass transition temperature associated with infinite molecular weight, and $\Psi(v_f)$ is a parameter related to free volume in the polymer systems. Larger free volume correlates with smaller T_g in Equation (3). In our case, we introduce a nanoparticle loading dependent function ϕ in Equation (2) to capture the effect of nanoparticle addition on polymer free volume change with a given molecular weight and temperature:

$$v_f = (A + BT + C/M) + \phi(NP\%), \qquad (4)$$

Based on the discussions above, the observed PCBM loading dependent PEO glass transition temperature changes (Figure 1c) suggest that $\phi(NP\%)$ and free volume v_f in PEO matrix gradually increase as the PCBM concentration increases from 0 to 20wt%, leading to decreased T_g and enhanced ion conductivity, while further increase of PCBM concentration from 20 to 40wt% only results in smaller $\phi(NP\%)$, smaller free volume v_f of PEO, increased T_g, and thus reduced ion transport performance.

The temperature dependent ion conductivity of PEO and salt based solid electrolytes can be modeled with the non-linear *Vogel-Tamman-Fulcher* (VTF) relationship (Equation 5) below a critical temperature, T_{critical}, to describe the coupling between ionic hopping and polymeric segmental motion, and with the log-linear Arrhenius dependency (Equation 6) above the T_{critical} to describe the decoupled ion transport from polymer segmental movements.[15, 17, 28, 33] The VTF relationship is expressed as:

$$\sigma = A\exp[-B/(T - T_0]/T^{0.5}, \qquad (5)$$

where A is the pre-exponential factor, B is the activation energy and T_0 is the equilibrium temperature associated with T_g of the polymer electrolyte material.[15, 17, 28, 33] The Arrhenius equation has the following form:

$$\sigma = \sigma_0 \exp(-E_a / kT) \quad (6)$$

where σ_o is the pre-exponential factor, E_a is the activation energy and k is the Boltzmann constant.[15, 17, 28, 33] The fitting results both above and below T_{critical} are listed in Table S1 and the fitted lines are shown as solid lines in Figure 1a. The T_{critical} of PEO/LiTFSI blend is reduced from 70°C (with no PCBM added) to 50°C for samples with 10 and 20wt% PCBM, and 45°C for sample with 40wt% PCBM. The trend of decreasing T_{critical} with increasing PCBM loading matches well with the corresponding changes in T_m described earlier, although the values of T_{critical} are 6-16°C larger than T_m, and thus more comparable to the onset of PEO melting process.

The activation energy E_a for the Arrhenius fit is increased from 4×10^{-20} J in pristine PEO/LiTFSI sample to $5\text{-}7\times10^{-20}$ J upon fullerene addition, which correlates with the reduced conductivity at higher temperatures (>70°C) in these fullerene-based composite electrolytes. In the VTF relation, the parameter B represents the activation energy of the coupled ion transport.[15, 17, 28, 33] The decreased parameter B from 895 in pristine PEO/LiTFSI to 375-470 for 10-40wt% PCBM blends compensates partially with the increased T_0 (from 249 in pristine PEO/LiTFSI to 269-273 in samples with 10-40wt% PCBM), yielding enhanced ion conductivity for PCBM incorporated blends. Since VTF relation is used to describe coupled ion transport from polymer segmental movement in lower temperature regions (below 45-70°C), [15, 17, 28, 33] enhanced ion transport below T_{critical} in samples with PCBM, especially in the blend with 20wt% PCBM, also suggest further decoupling between ion transport and polymer segmental motion.

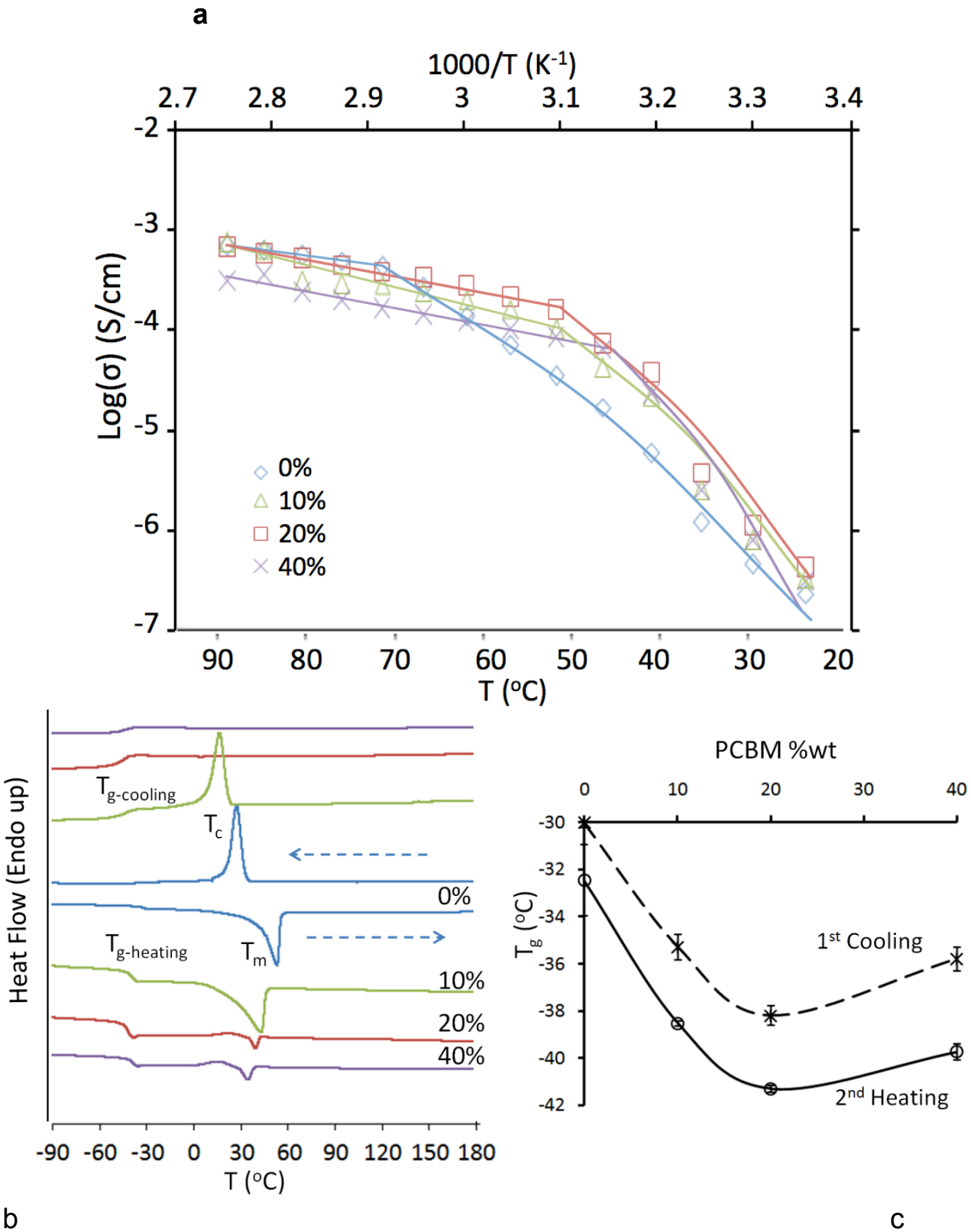

Figure 1. a). Temperature dependence of ionic conductivities in PEO-LiTFSI (10:1) electrolytes as a function of added PCBM weight percentage (0- 40wt%). A typical conductivity

measurement in this work has ~5% variation as experimental error, which is too small to show up in the logarithmic plot. The temperature dependent ion conductivity of PEO and salt based solid electrolytes can be modeled with the non-linear Vogel-Tamman-Fulcher (VTF) relationship (Equation 5) below a critical temperature, $T_{critical,}$ to describe the coupling between ionic hopping and polymeric segmental motion, and with the log-linear Arrhenius dependency (Equation 6) above the $T_{critical}$ to describe the decoupled ion transport from polymer segmental movements. Arrhenius and VTF fitting of the *log* (conductivity) vs. *1000/T* are performed at temperatures higher or lower than the $T_{critical}$ (solid lines). The fitting parameters are listed in Table S1. b). The 1st cooling and 2nd heating DSC scans of PEO/LiTFSI blends as a function of added PCBM content. c). Recorded glass transition temperature as a function of PCBM weight percentage.

The impedance spectra for the PEO/LiTFSI blends at 30°C are presented in the Nyquist plot as a function of PCBM concentration (Figure 2a). The spectra exhibit semicircle shape followed by a straight line, which is in agreement with blocking electrode response.[34] The equivalent circuit modeling results (shown as solid lines) are based on the $((R_{Bulk}(R_{GB}C_{GB}))C_{Bulk})C_{DL}$ circuit model[2] shown as the inset of Figure 2a and the corresponding χ^2 values are $0.8\text{-}3\times10^{-2}$. In this circuit model for PEO-lithium salt blends,[2] R_{Bulk} and R_{GB} are the resistance in electrolyte bulk (i.e. highly conductive amorphous PEO regions) and grain boundaries (less conductive regions such as PEO crystallites), while C_{DL}, C_{Bulk} and C_{GB} represent the double layer capacitance as well as the capacitance in bulk and grain boundaries, respectively. Capacitance (C) and resistance (R) elements obtained from equivalent circuit modeling are further converted into conductivity (σ) and permittivity (ε) after normalization against thickness and area. The temperature dependent behaviors of the equivalent circuit modeling results are shown in Figure 2 b-c as well as in Figure S1 and S2. The value of ε_{DL} has a slight dependence on temperature and fullerene loading, with values of fullerene-loaded electrolytes similar to each other and 2-10 times lower than those of pristine films. This indicates that the incorporation of PCBMs contributes towards a reduced electrical double layer effect at electrode-electrolyte interfaces, possibly because of the interfacial distribution of PCBMs. For the bulk components of the circuit

model, ε_{Bulk} and dielectric constant ($k= \varepsilon / \varepsilon_{Vacuum}$) of the bulk components are almost insensitive to fullerene loading and temperature in the range of 30-80^{o}C, while σ_{Bulk} in fullerene based electrolytes, especially in the one with 20%wt PCBM, show up-to-an-order-of-magnitude improvement as compared to the pristine system. These observations suggest that, even in the highly ion conductive, amorphous regions of the pristine PEO-LiTFSI blends, the low-temperature (< 80^{o}C) ion conductivity can be further improved with the addition of fullerenes, and the ion polarization behaviors in the bulk domains are relatively unchanged. For the grain boundary components in the circuit model, ε_{GB} and the corresponding dielectric constant are reduced by up to 3 orders of magnitude in fullerene incorporated blends, while σ_{GB} only shows irregular changes with increased fullerene content. These results may be attributed to the participation of fullerenes in grain boundaries and the reduced free ion components of the grain boundary regions.

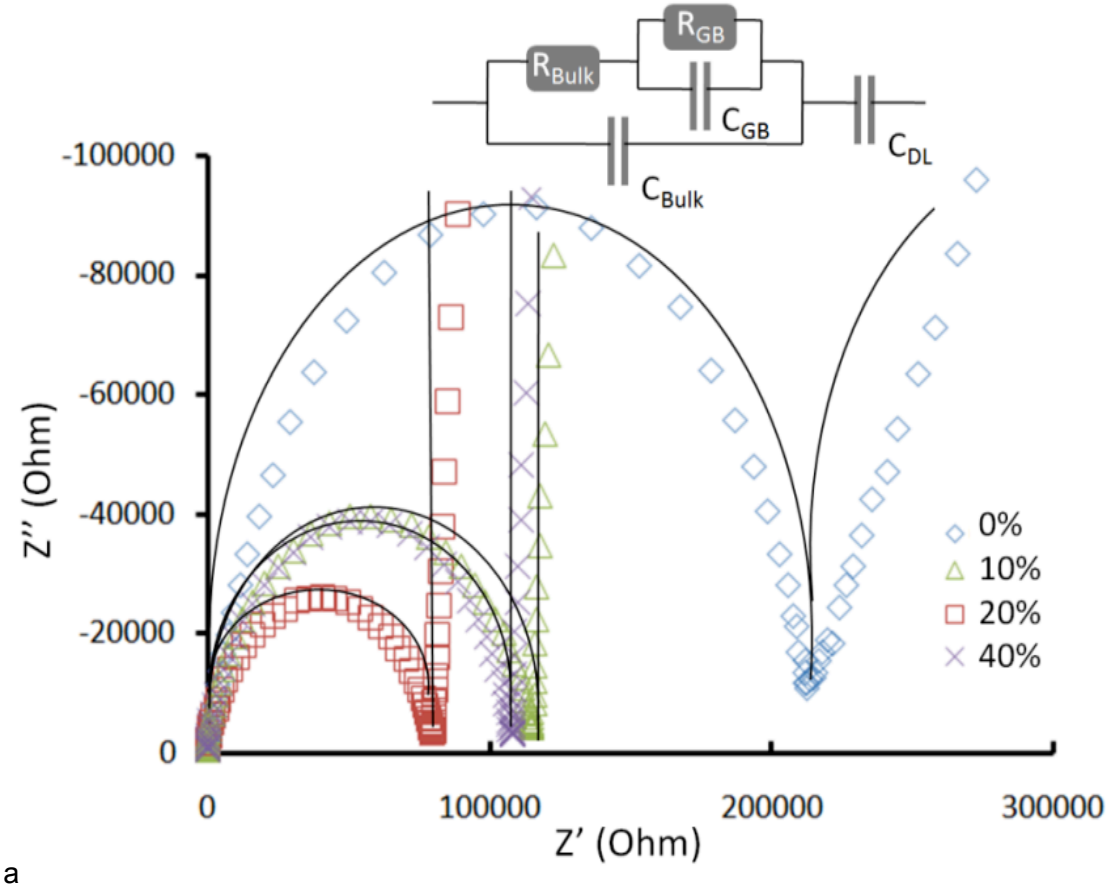

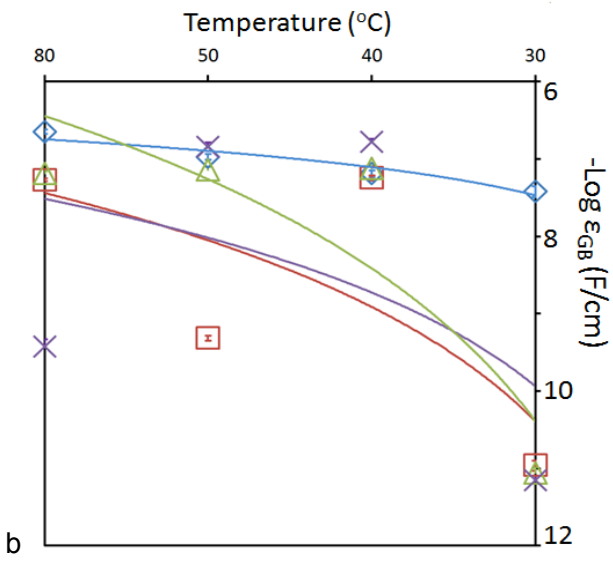

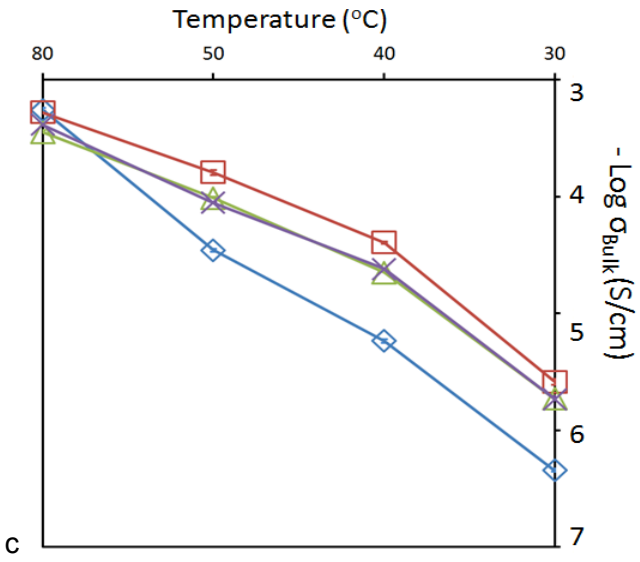

Figure 2. a). Nyquist plots of PEO-LiTFSI (O:Li=10:1) electrolytes in blocking electrode cell as a function of PCBM concentration (0, 10, 20 and 40wt%) at 30°C. The solid lines are fitting results from equivalent circuit modeling using the model circuit [2] shown as inset. R_{Bulk} and R_{GB}

stand for the resistance in bulk and grain boundaries. C_{Bulk} and C_{GB} represent the capacitance in bulk and grain boundaries. Additionally, C_{DL} is the double layer capacitance. b-c). Selected fitting results (ε_{GB} and σ_{Bulk}) of equivalent circuit modeling as a function of PCBM loading and temperature. Additional fitting results are available in Figure S1 and S2.

To study the mechanical properties of PEO-LiTFSI blends upon PCBM addition, nanoindentation was used to extract elastic modulus and hardness of the composite electrolyte films (Figure 3). The elastic modulus and hardness of the PEO-LiTFSI blends before PCBM addition are 140±5 MPa and 5.3±0.3 MPa, respectively. The addition of 10-20wt% PCBM decreases these values to 50±4 and 60±10 MPa, 1.7±0.3 and 1.5±1.2 MPa, respectively. At 40wt% PCBM, the elastic modulus and hardness of the blend are further reduced to 20±3 and 0.14±0.05 MPa. Our Young's modulus value of PCBM-free sample measured at room temperature (140 MPa) is comparable to the values reported by Cimmino and coworkers [35] where they found the Young's modulus of PEO materials with different molecular weight ranged between 108 and 137 MPa. The descending trend of Young's modulus with addition of PCBM can be attributed to the increase free volume and decreased crystallinity.[36] The crystal structure and crystallinity changes will be discussed in details below. The modulus of PCBM-based electrolytes is still much higher than those of typical gel based electrolytes (1-5 MPa by tensile [37]). The highly tunable mechanical properties (20-140 MPa in modulus) achieved in this work can potentially enable both rigid (solid) and flexible (semi-gel) electrolyte system, simply via systematic manipulation of fullerene loading.

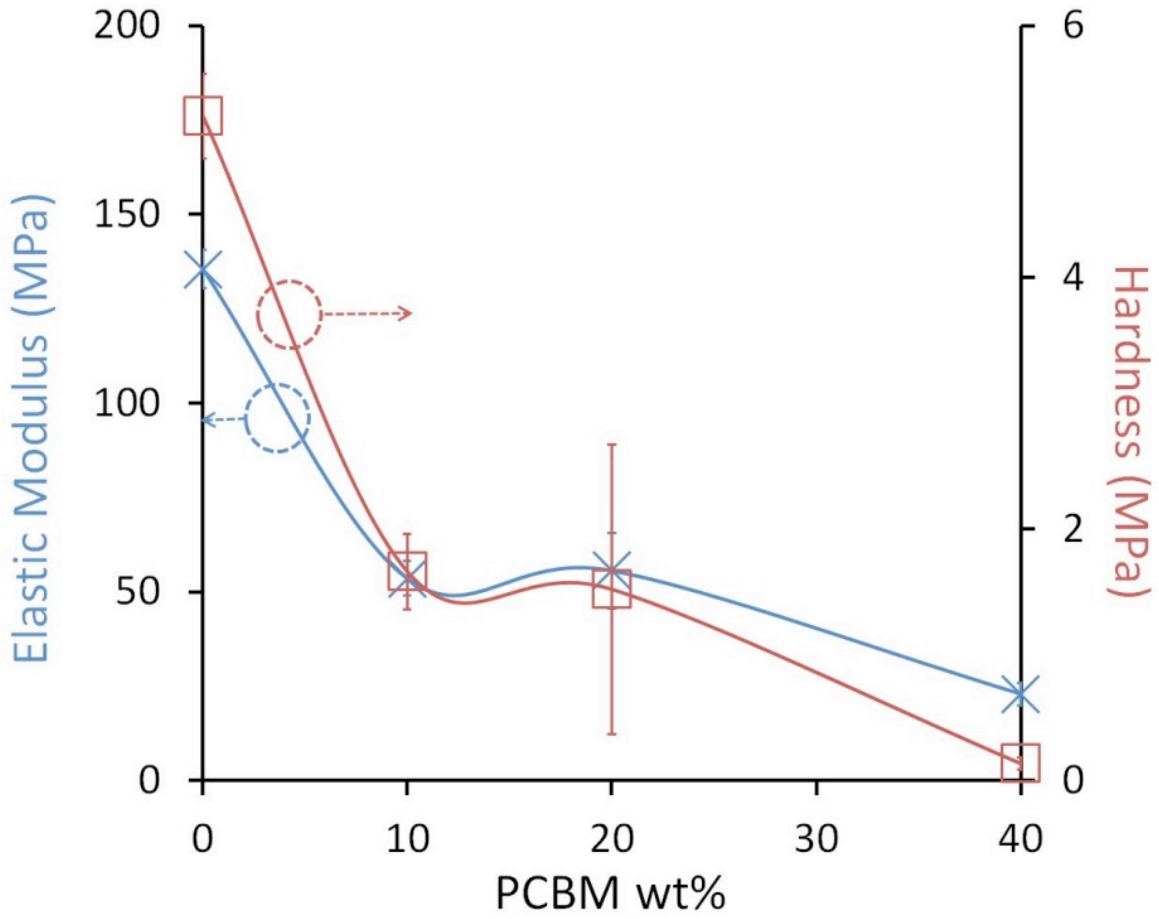

Figure 3. Hardness and elastic modulus of PEO-LiTFSI (10:1) electrolytes as a function of PCBM weight percentage (0-40wt %) as determined by nanoindentation experiments.

X-ray diffraction results of the PEO-LiTFSI blends are given in Figure 4. Based on reported results on PCBM,[38-40] PEO and $P(EO)_6LiTFSI$,[29] the obtained experimental reflections of X-ray spectra are labeled with "M", "O", and "X", for contributions from PCBM, pure PEO, and $P(EO)_6LiTFSI$, respectively. It is noted that the Bragg peaks from pure PEO-LiTFSI blend are made up of the ones from pure PEO and $P(EO)_6LiTFSI$ salt-polymer complex, in agreement with previous reports [26-29]. These peaks are considerably suppressed at 10wt% or 20wt% PCBM loading, while reflections from PCBM crystals gradually show up. Finally, at 40wt% PCBM loading, PCBM reflections become dominating.

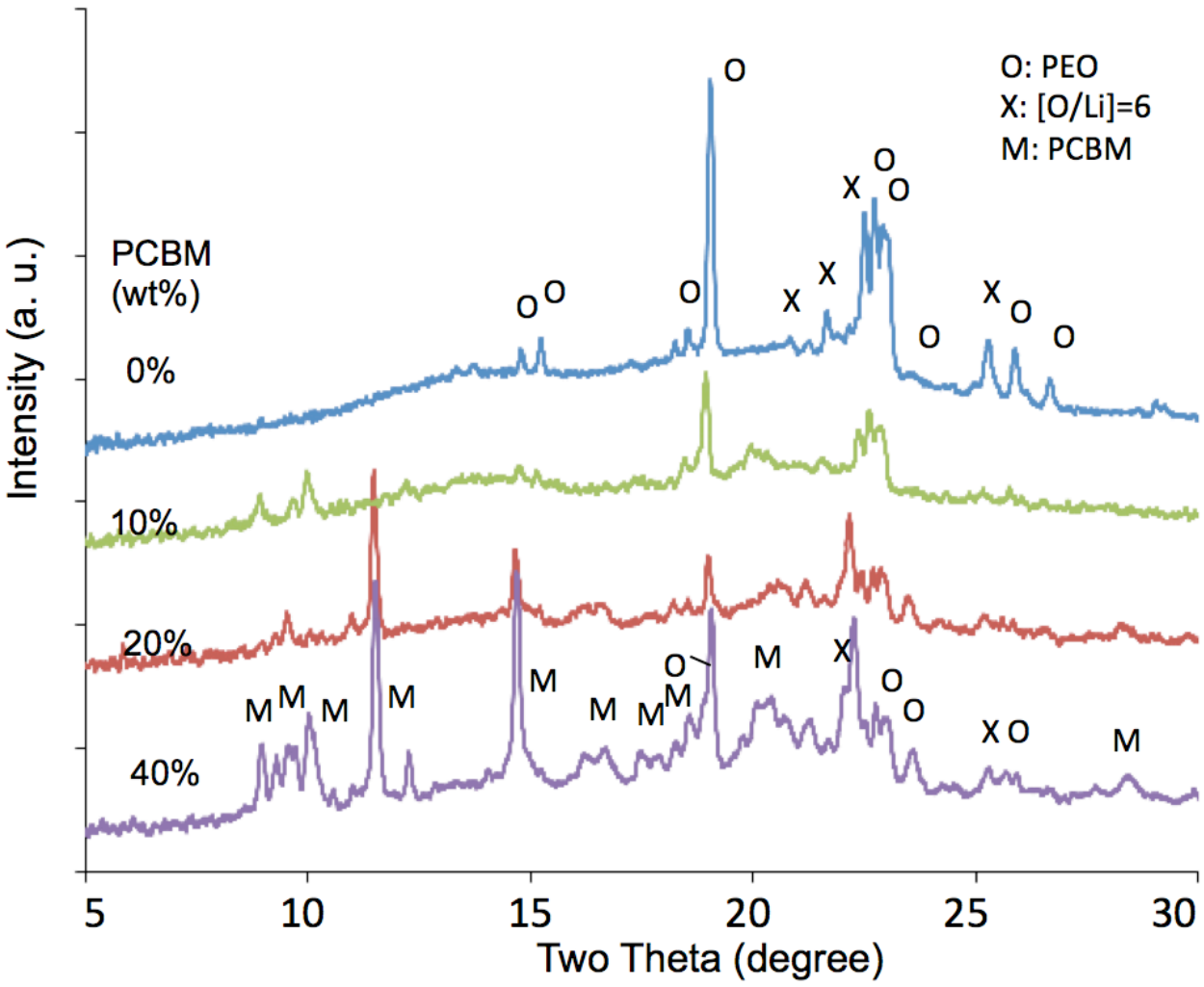

Figure 4. X-ray diffraction results of PEO-LiTFSI (10:1) electrolytes as a function of PCBM weight percentage (0- 40wt%). The peaks from pure PEO are labeled with open circle, and the ones from the $(PEO)_6$:LiTFSI complex are marked with "X". The reflections from PCBM are labeled with "M".

Selected area electron diffraction patterns (SAED) (Figure 5a) of the blend systems suggest a strong PCBM concentration dependence similar to the trend observed in X-ray diffraction experiments. The pure PEO/LiTFSI sample has distinctive sharp reflections, for example, (-212) from PEO crystals, based on reported PEO unit cell[41-42] Since the PEO crystal sizes in PEO/LiTFSI blends are significantly smaller than the selected area diffraction aperture used (~1

micron in diameter), they yield diffuse ring or arc-shaped diffraction patterns. These crystalline PEO reflections are largely diminished at PCBM concentrations of 10-40wt% in SAED patterns. On the other hand, the PCBM *d* spacing of 0.46nm becomes stronger with increased amount of added PCBMs. In particular, with PCBM loading of 40wt%, the 0.46nm ring becomes much sharper and stronger than those in samples with 10 -20wt% PCBM additions, as shown in the 1-D intensity vs. two theta plots in Figure 5b. This implies that the PCBM packing in the 40wt% PCBM blend is considerably more regular as compared to other compositions.

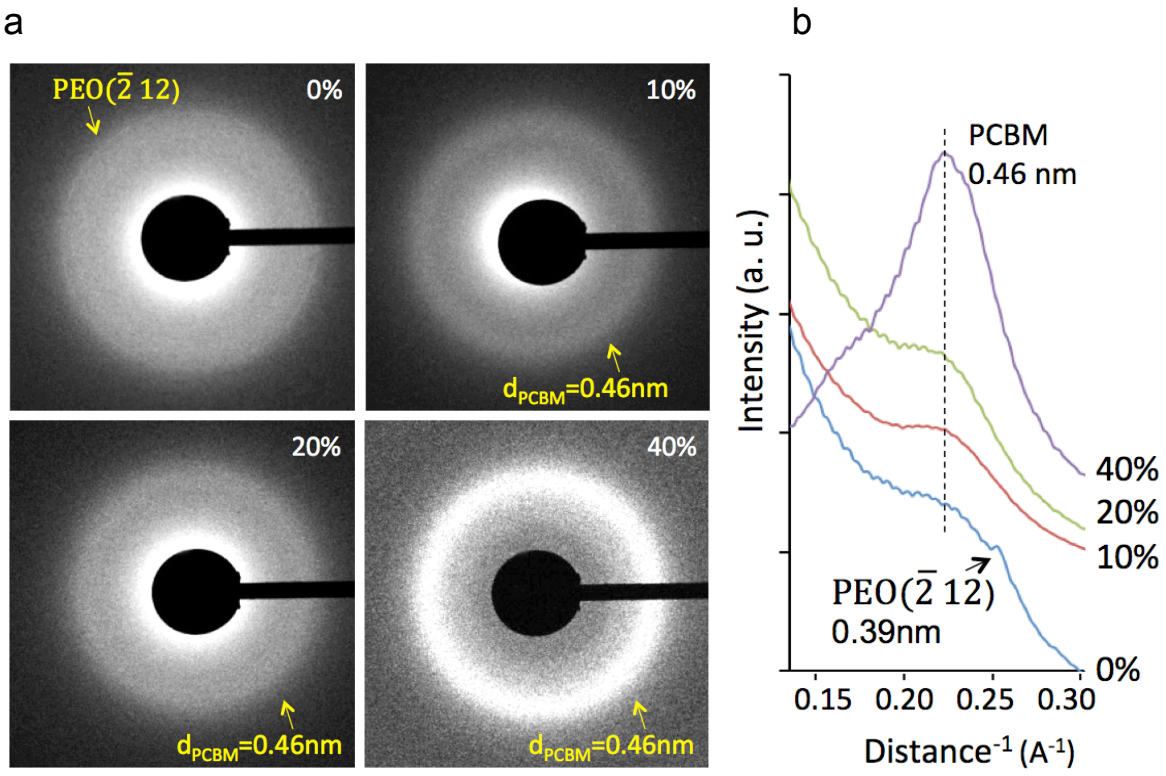

Figure 5. a.) Selected area electron diffraction patterns of PEO-LiTFSI ([O:Li]=10:1) blends as a function of the added PCBM concentration (0-40wt%). b). One-dimensional azimuthally-averaged radial profiles are given on the right.

To investigate the nanoscale salt-polymer distribution as a function of PCBM loading, energy-filtered TEM (EFTEM) was performed using drop-cast films on ultrathin carbon supported copper grids with minimal air exposure (Figure 6). Although the drop-cast method used here involves thickness variations of the deposited film (resultant from their film drying processes), they do not interfere with EFTEM image analysis. Thickness maps of representative samples are shown in Figure S3, allowing us to fully monitor the thickness effect. Figure 6a-d show elastic (0±4eV) images of PEO-LiTFSI blends ([O:Li]=10:1) as a function of PCBM weight percentage (0, 10, 20, and 40wt%). Combined oxygen (red) and sulfur maps (green) of the blends with 0, 20, and 40wt% are shown in Figure 7a-c. Since PCBM has a strong plasmon peak at 30eV [43], an image with 30±4eV energy window is shown in Figure 7d to highlight the location of PCBM clusters for the electrolyte systems with 40wt% PCBM. It is observed that the original PEO/LiTFSI blend has distinctive oxygen- (PEO-), or sulfur- (salt-) rich regions (>50nm in size), corresponding to a phase separated PEO/PEO-Li complex system [26-29] and a low ion conductivity at room temperature. Further quantitative analysis of sulfur and oxygen maps (Figure 7e) supports this argument. As the PCBM concentration increases to 10-20wt%, the well-dispersed PCBMs lead to well mixed PEO-salt blend, corresponding to their significantly enhanced room-temperature ion conductivity. The circles in Figures 6d and 7d highlighted some typical PCBM cluster formation in the composite electrolytes with 40wt% PCBM.

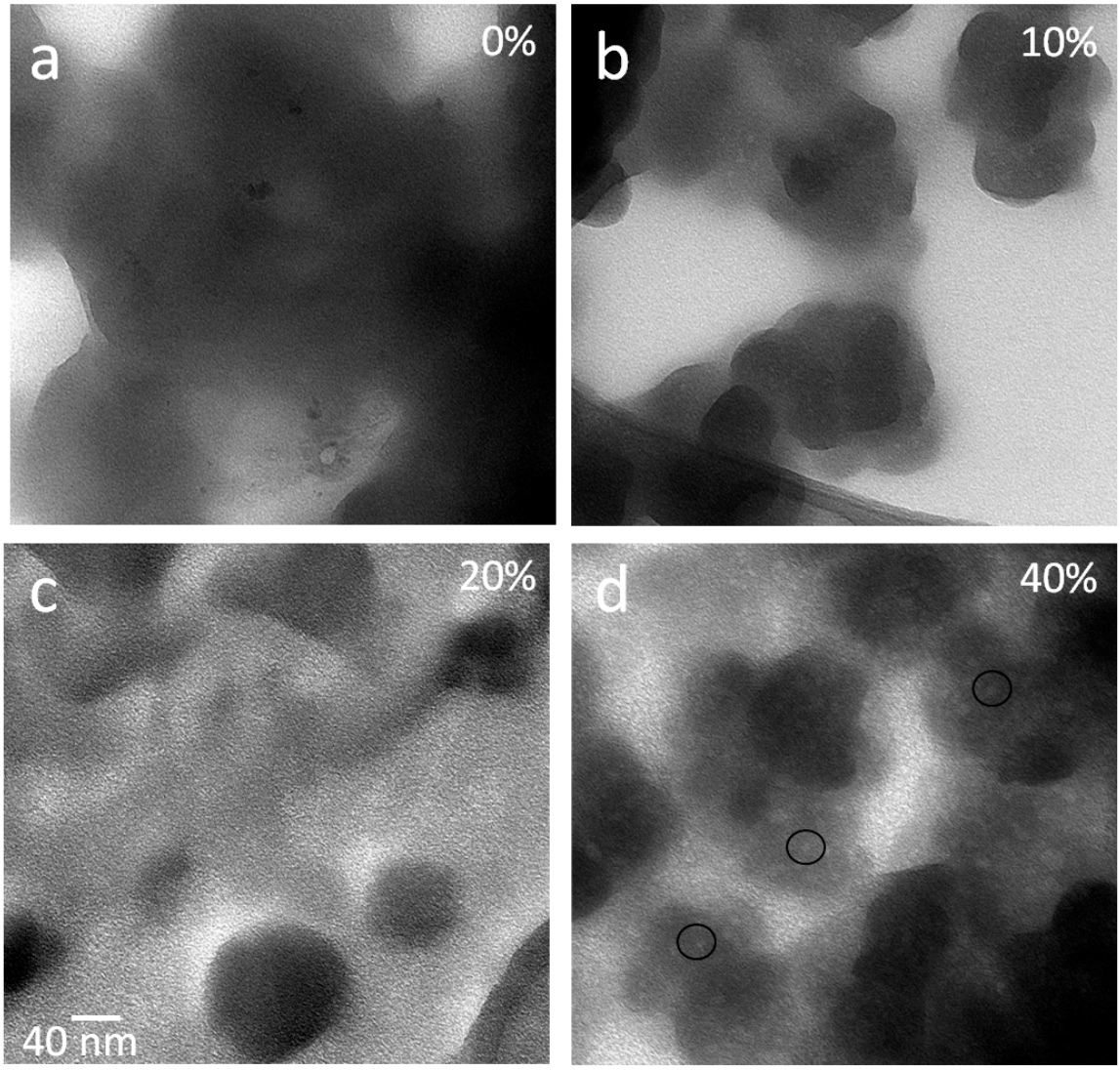

Figure 6. Elastic images (0±4eV) of PEO-LiTFSI ([O:Li]=10:1) electrolytes as a function of added PCBM weight percentage in energy filtered TEM. Three aggregated PCBM domains in Figure 6d are identified with circles, which are also revealed in 30±4eV image (Figure 7d). Figure 6d and Figure 7d are taken from the same sample area. In addition, the imaging locations of Figure 6 a, c, and d correspond to the ones in Figure 7 a, b, and c (composite elemental maps). All TEM micrographs share the same scale bar of 40 nm in Figure 6c.

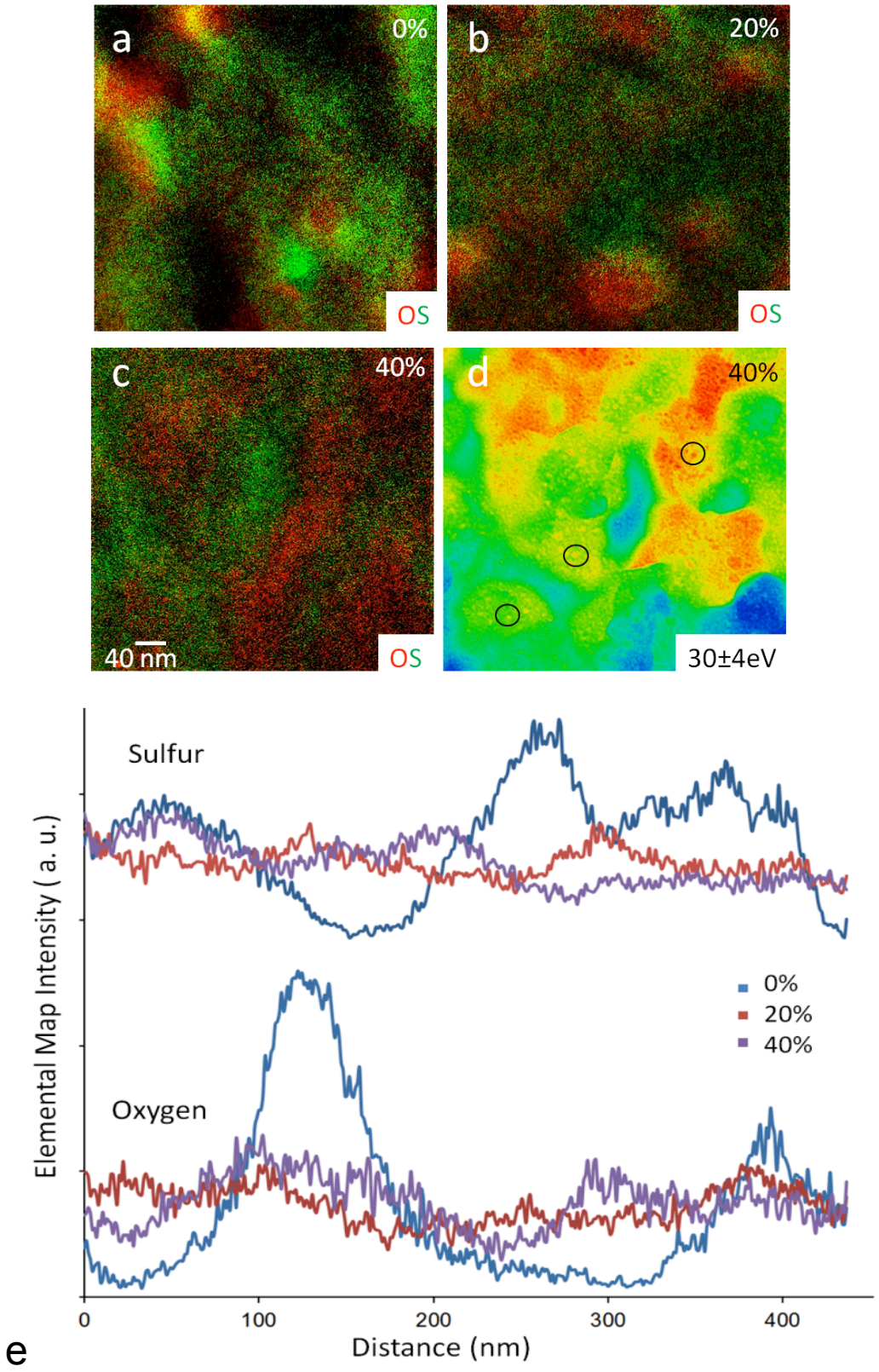

Figure 7. PEO-LiTFSI ([O:Li]=10:1) electrolytes with varied PCBM weight percentage (0-40%) in composite elemental maps (a, b, c) and 30±4eV image (d) by energy filtered TEM. Figure 7a-

c give combined oxygen (red) and sulfur maps (green). Figure 7d shows an image with 30±4eV, corresponding to the 0±4eV image in Figure 6d, and highlights the locations of PCBM clusters with brighter colors for the blend electrolyte system with 40wt% PCBM, with the circles marked three aggregated PCBM clusters. e). Typical line scans of EFTEM images (sulfur and oxygen maps) shown in Figure 6 as a function of PCBM percentage. All TEM micrographs share the same scale bar of 40 nm in Figure 7c.

Quantification of nanodomains observed in 30eV low plasma EFTEM imaging is performed by grayness scale line scan analysis as shown in Figure 8a and 8b. For each blend (0, 10, 20 and 40wt% PCBM), 56 domains are measured and plotted in this analysis. Based on these quantifications, the average domain sizes increase from 3.4±0.9 nm in the pristine PEO/LiTFSI blend, to 4.6±1.2 nm in the blend with 10wt% PCBM, 4.9±2.0 nm in the one with 20% PCBM, and finally to 7.5±4.5 nm in the sample with 40wt% PCBM blend. It is noted that, when the domain size is lower than 3-4 nm, a precise PCBM domain dimension may not be identifiable in the current EFTEM study because of background noise as well as their lack of contrast in PEO matrix under low eV plasma imaging conditions. Higher magnification EFTEM and more accurate determination of the dimensions of those smaller nanodomains (<3 nm) are experimentally challenging because of the beam sensitivity of the polymer electrolyte samples under the available experimental setup. Nevertheless, the 30eV plasma imaging enables accurate and systematic quantifications of the majority of nanodomain sizes (4-25 nm) observed in this study.

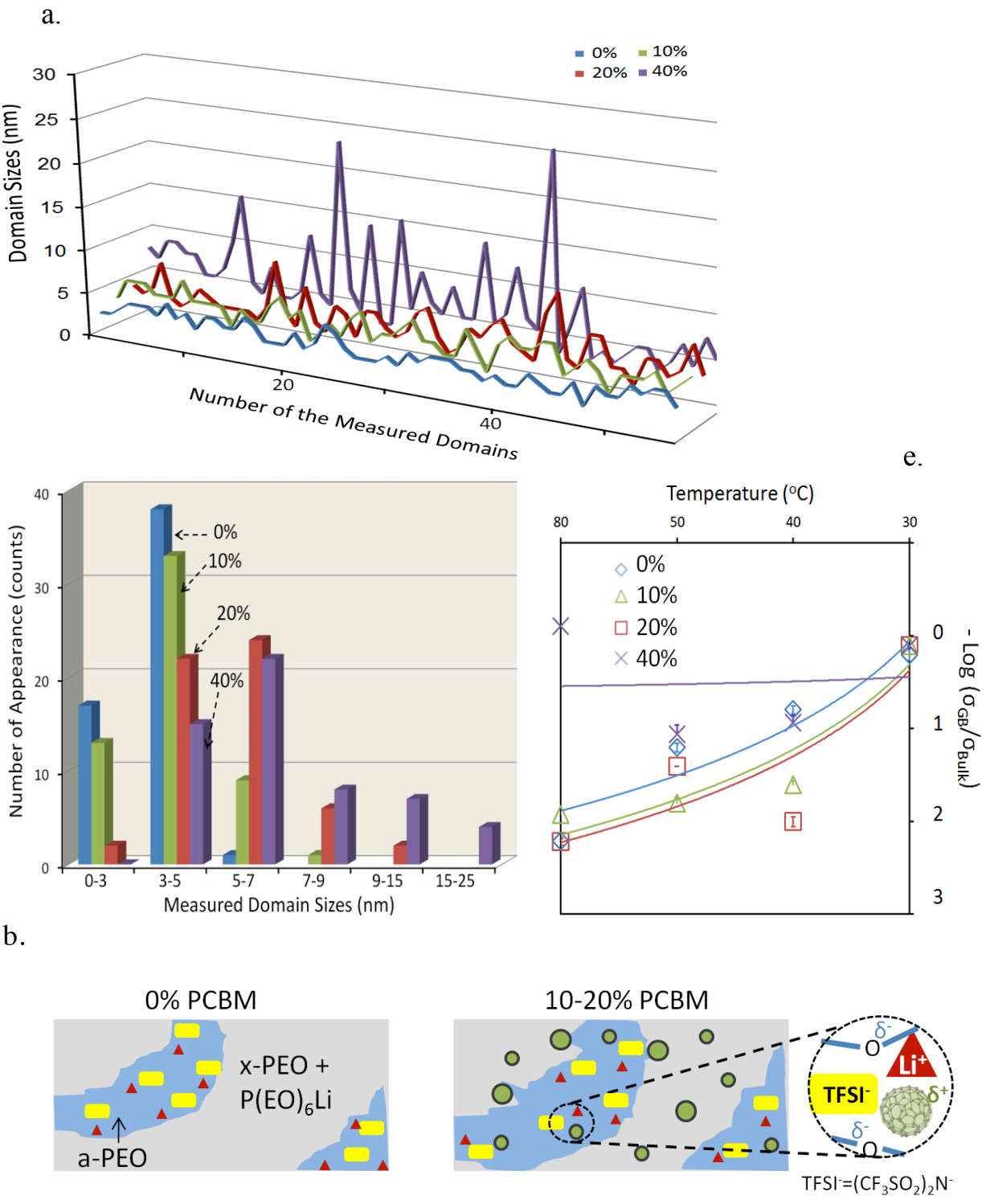

Figure 8. Measured nanodomain sizes (a) and distributions (b) from 56 domains of each PEO-LiTFSI blends (with 0-40wt% PCBM). The size analysis is based on line scans of 30eV plasma EFTEM images. The pristine PEO/LiTFSI sample was also measured to serve as a background

reference. It is noted that, when the domain size is lower than 3-4 nm, a precise PCBM domain dimension may not be identified because of the background and lack of contrast in well dispersed PCBM-PEO matrix. Figure 8c, d are schematics showing the effects of PCBM addition. Amorphous PEO (a-PEO), crystalline PEO (x-PEO) and PEO-LiTFSI crystalline complex ($P(EO)_6Li$) regions are highlighted with different colors and labels. The green circles represent PCBM clusters with different aggregation sizes. The effect of PCBM addition on temperature-dependent grain boundary/bulk conductivity ratio in log arithmetic scale is based on equivalent circuit modeling results from this work (e).

According to a calculation based on density functional theory, [44] the interaction energies between PEO and PEO is 2.58 kcal mol^{-1} per monomer, while the corresponding value is 3.50 kcal mol^{-1} per monomer for interactions between PCBM and PEO, and 6.01 kcal mol^{-1} per monomer for PCBM and PCBM. This indicates that at a low PCBM loading (or when it is difficult for PCBM to find another PCBM to interact with), PCBM is likely to disperse well in PEO matrix because the PCBM-PEO interaction is slightly stronger than the PEO-PEO interaction, whereas at a high PCBM concentration, the PCBM is more likely to pack with other PCBM into aggregated domains, as we observed experimentally in this work.

Two schematics in Figure 8c, d are drawn to showcase the effect of PCBM addition. The pristine PEO/LiTFSI electrolyte has significant PEO and $P(EO)_6$LiTFSI salt complex crystallinities, which are largely reduced upon PCBM addition. PCBM is partially electron-withdrawing, which can compete with lithium cations in attracting TFSI anion and interacting with polyethylene oxide. Participation of PCBMs at both amorphous conductive regions (bulk) and grain boundaries are expected. The addition of PCBM also induces systematic changes in crystallinity and crystal dimension, free volume of the polymer matrix, grain boundary and bulk conductivity, double layer and grain boundary permittivity as well as decoupling of ion transport and PEO

segmental movements. Those complex changes and enhanced ion transport are achieved through a distribution of PCBM nanocluster formation with average sizes of 3-10 nm. The ratio of grain boundary and bulk conductivity (σ_{GB} /σ_{Bulk}) from equivalent circuit modeling is used in Figure 8e as a figure of merit to highlight the temperature-dependent correlation between PCBM concentration and ion transport in these systems. A lower value of log(σ_{GB} /σ_{Bulk}) corresponds to higher ion conductivities in amorphous PEO regions than the ones in crystalline PEO or PEO/Li complex. The volume and connectivity of grain boundary and grains are among other important factors, which are difficult to quantify here.

To elaborate on the observed systematic interplay between nanomorphology and various properties of PCBM based nanocomposite electrolytes, here we will individually discuss the correlations between **(1)** nanostructure and mechanical properties, **(2)** nanostructure and thermal properties, **(3)** nanostructure and electrical properties, as well as **(4)** mechanical and electrical properties.

(1) The demonstrated correlations between mechanical properties and microstructures are intriguing. For example, it is noticed that when the PCBM content is below 30wt%, both the elastic modulus and hardness have a trend to decrease first and then increase with increasing PCBM loading. It is reasonable to expect that PCBM aggregation can contribute towards increased mechanical properties, while decreased polymer matrix crystallinity will result in reduced mechanical properties. Therefore, the overall effects of the two combating factors yield the observed complex, nonmonotonic and nonlinear behaviors in elastic modulus and hardness as a function of PCBM loading.

(2) Because the X-ray diffraction and micrsocopy experiments in this work are performed at room temperature, the interplay between electrolyte nanostructures and their corresponding thermal properties is mainly probed by DSC (Figure 1b-c) and equivalent circuit modeling of variable temperature

impedance spectra (Figure 2 and Figure S1-S2). The bulk components in equivalent circuit models correspond to amorphous PEO matrix with higher ion conductivity, while the grain boundaries in these models correspond to less ion-conductive, crystalline complex of PEO and lithium salt. By following the trends of permittivity and conductivity at grain boundaries and in bulk as a function of temperature, it is made possible to indirectly estimate the relative changes of amorphous PEO, crystalline PEO/salt complex, and PCBM aggregation at different temperatures, with linkages to their important thermal transitions and free volume changes. **(3)** The interdependent relationships of nanostructure formation and electrical properties are the main focus of this work, which is enabled by the clean surface chemistry and monodispersity of PCBM additive. The enhanced ion conductivity achieved in this work is interpreted through both real space and reciprocal space methods, along with equivalent circuit modeling. Although it is extremely difficult to establish one-to-one correlation between what is observed in X-ray diffraction, energy filtered TEM analysis, and equivalent circuit models, we are able to gain an overall pictures of what is happening at various length scales and understand the basis of ion conductivity enhancement in the PCBM based electrolytes from various perspectives. **(4)** It is demonstrated in this work that, depending upon the specific nanostructure formation involved, mechanical properties of a nanocomposite system have rather complicated correlations with their electrical properties, which can be desirable in terms of providing tunability for flexible battery designs. The broad range of mechanical and electrical properties achieved in this work could contribute towards both gel-based and solid polymer electrolytes.

The electron conductivity of fullerene derivative could play a role in the overall performance of the nanocomposite electrolytes. As we mentioned earlier in the introduction section, PCBM is known as an n-type, electron-transporting semiconductor, therefore it is expected that PCBM will not contribute significantly to the leakage current of the electrolyte systems. Our equivalent circuit modeling results indicated that PCBM improved the permittivity and conductivity of the grain boundaries and bulk components in the nanocomposite electrolytes, with no signs of performance deterioration. Furthermore, as illustrated in the inset of Figure 8d, the electron-withdrawing nature of the “Bucky ball” could make

PCBM attractive to TFSI anion and PEO matrix, which in theory can contribute towards less tightly bonded lithium ion, easier charge hopping, and decoupled ion transport. Our variable temperature conductivity measurement and analysis partially support this hypothesis.

The comprehensive effects of the polymer-matrix molecular weight and polydispersity could be a subject of future research, towards further optimization of the nanocomposite electrolytes with PCBM additives. Molecular weight and polydispersity of the polymer matrix will likely to affect PCBM aggregation formation, ion conductive grain and boundary structures, coupling or decoupling of ion transport and polymer backbone dynamics, as well as many other closely involved issues in these electrolyte systems. They could provide further tunability on ion conductivity and other desirable properties, but the study of those effects is outside of the scope of the current work.

Because fullerene has no Lewis acidic sites on their surface, it is concluded that the enhancement of ion transport enhancement observed in this work is solely resulted from nanoparticle-induced changes in polymer matrix. This work thus provided a unique example of performance enhancement in nanocomposite electrolytes with no Lewis acidic sites and nanoparticle surface treatment. In addition, this work presented a systematic interplay between nanomorphology and various properties of nanocomposite electrolytes (including mechanical, thermal, and electrical properties), with well defined nanoparticle surface chemistry as well as nanoparticle size and distribution, which is extremely difficulty (if not impossible) to achieve in oxide nanoparticle based electrolytes.

In summary, we introduced fullerene based polymer nanocomposite electrolytes as a new class of solid polymer electrolytes and examined their nanostructure-property relationships as a

function of temperature and fullerene loading. Up to 600% ion conductivity enhancement was achieved in PEO/LiTFSI systems, and correlated with changes in PEO free volume, crystallinity and crystal dimension, and nanoscale morphology. The improved ion transport was further linked to systematic changes in mechanical properties, decoupling between ion transport and polymer segmental motions, as well as conductivity and permittivity at grain boundaries and in bulk upon PCBM addition. The advances in chemistry recently made important progress towards functional supramolecular assemblies of fullerenes in polymer hosts and even fullerene-based block copolymers.[45-46] Self-assembly of those supramolecular and block copolymers with fullerene component has made important impacts on organic optoelectronic materials, [21, 45-46] but is not yet explored in the context of solid polymer electrolytes. The marriage of fullerene derivatives and polymer electrolytes could open up exciting opportunities for optimizing the nanostructure and ion transport of solid polymer electrolytes.

Experimental

Film Preparation. PEO (Mn=270k, PDI=1.1) is synthesized using potassium *tert*-butyloxide as the initiator and high-vacuum all-glass anionic polymerization technique. [47] PCBM is used as received from Sigma Aldrich. LiTFSI is purchased from Sigma Aldrich and dried at 120^{o}C in glove box for 2 days before use. Desired amount of dry PEO, LiTFSI, and PCBM were dissolved in anhydrous THF, followed by drying in a vacuum oven for three-to-four days and being stored in argon-filled glove box.

Impedance Spectroscopy and Equivalent Circuit Modeling. The polymer-LiTFSI samples were pressed into the disc with 1/4" diameter and 1/32" thickness at elevated temperature (60^{o}C for PEO and 200^{o}C for the blended polymers) under argon gas filled environment. The disc samples were subsequently assembled into a coin cell configuration for the conductivity measurement in the glove box. In the cell, the disc sample was sandwiched by stainless spacers under a spring load. A 15 mil thick Teflon ring was placed between the spacers to prevent the electronic shorting as well as constrain the volume expansion of the sample. As soon as the cell leaves the argon environment, epoxy was applied to seal the edge of the cell to minimize the moisture contamination. Copper wires were attached to each side of the cell with silver epoxy to build the electronic connection. The Ohmic resistance between the cell and copper wire was checked with the multi-meter to ensure the contact resistance is negligible. The conductivity of the sample was monitored at room temperature for at least 7 days until the steady state was reached. During the testing, the cell was placed in the close-top Teflon heating block for temperature control. The testing temperature starts from 25^{o}C to 90^{o}C with 5^{o}C increment and the measurement was conducted after 2 hrs of temperature equilibration. The impedance measurement was performed using Solartron 1260 (Impedance/gain phase analyzer) and 1286(Electrochemical interface) combo. The voltage perturbation was applied at 10 or 50mV amplitude as a function of frequency from 10MHz to 0.1Hz. The sample dimension was obtained by taking the cell apart in the glove box after testing.

Differential Scanning Calorimetry. Differential scanning calorimetry measurements were performed using TA instruments (Q1000) with a heat/cool/heat protocol under nitrogen flow in sealed aluminum pans. Samples (2-4 mg) were preheated to 200^{o}C to remove thermal history,

then cooled to -100°C, and finally re-heated to 200°C with a ramp rate of 10°C/min. The first cooling and the second heating cycles were used to determine transition temperatures.

Nanoindentation. Nanoindentation was performed on a TriboIndenter (Hysitron Inc. Minneapolis, MN) using a displacement control mode. Elastic modulus and hardness values were calculated from the unloading curve according to the Olive and Pharr method.[48] For each sample, the peak penetration was fixed at 500 nm, with a loading time and an unloading time of 5 seconds, respectively. The mean and standard deviation in the elastic modulus and hardness were determined from indentation tests performed on five different locations on the sample surface for all samples.

X-ray Diffraction (XRD). XRD experiments of the nanocomposites electrolyte films were performed on a Panalytical X'Pert with a copper K-alpha radiation. The samples are sealed in air-tight plastic bags before each experiment.

Transmission Electron Microscopy (TEM). Dilute anhydrous THF solutions (0.2wt%) of nanocomposite electrolyte were drop cast on amorphous carbon supported copper grids. The drop-cast films are isolated from air and moisture except a brief exposure during TEM sample loading. (Both room-temperature and cryo-microtoming involves extended exposure to air and moistures, which is not pursued in this work). Energy filtered TEM experiments and selected area electron diffraction were conducted in a Zeiss Libra 120 equipped with an in-column Omega energy filter. An acceleration voltage of 120kV and emission current of ~5×10^{-6}A were used in order to minimize electron damage to polymer based samples.

Acknowledgement

This research was conducted at the Center for Nanophase Materials Sciences, which is a DOE Office of Science User Facility. D. Li acknowledges travel support from NSF under award #ECCS-1151140.

Reference

1 F. Croce, G. B. Appetecchi, L. Persi, B. Scrosati, *Nature* 1998, **394**, 456-458.
2 G. B. Appetecchi, F. Croce, J. Hassoun, B. Scrosati, M. Salomon, F. Cassel, *J. Power Sources* 2003, **114**, 105-112.
3 H. M. Xiong, X. Zhao, J. S. Chen, *J. Phys. Chem. B* 2001, **105**, 10169-10174.
4 A. Karmakar, A. Ghosh, *J. Nanoparticle Res.* 2011, *13*, 2989-2996.
5 J. Chen, C. D. Frisbie, F. S. Bates, *J. Phys. Chem. C* 2009, **113**, 3903-3908.
6 A.A. Teran, M.H. Tang, S.A. Mullin, N.P. Balsara, *Solid State Ionics* 2011, **203**, 18-21.
7 A. Panday, S. Mullin, E.D. Gomez, N.S. Wanakule, V.L. Chen, A. Hexemer, J. Pople, and N.P. Balsara, *Macromolecules* 2009, **42**, 4632-4637.
8 F. S. Fiory, F. Croce, A. D'Epifanio, S. Licoccia, B. Scrosati, E. Traversa, *J. Europ. Ceram. Soc.* 2004, **24**, 1385-1387.
9 X. Liu, T. Osaka, *J. Electrochem. Soc.* 1996, **143**, 3982-3986.
10 Y. Yin, "An Experimental Study on PEO Polymer Electrolyte Based All-Solid-State Supercapacitor" 2010 *Open Access Dissertations of University of Miami*.
11 P.K. Singh, R.K. Nagarale, S.P. Pandey, H.W. Rhee, B. Bhattacharya, *Adv. Nat. Sci.: Nanosci. Nanotechnol.* 2011, **2**, 023002.
12 J. H. Ahn, G. X. Wang, H. K. Liu, S. X. Dou, *J. Power Sources* 2003, **119-121**, 422-426.
13 S. K. Fullerton-Shirey, J. K. Maranas, *J. Phys. Chem. C* 2010, **114**, 9196-9206.
14 W. Krawiec, L. G. Scanlon, J. P. Fellner, R. A. Vaia, E. P. Giannelis, *J.Power Sources* 1995, **54**, 310-315.
15 C. W. Nan, L. Z. Fan, Y. H. Lin, Q. Cai, *Phys. Rev. Lett.* 2003, *91*.
16 Y. Liu, J. Y. Lee, L. Hong, *J. Appl. Polym. Sci.* 2003, **89**, 2815-2822.
17 T. J. Singh, S. V. Bhat, *J. Power Sources* 2004, **129**, 280-287.
18 H. W. Chen, C. Y. Chiu, F. C. Chang, *J. Polym. Sci. Part B-Polym. Phys.* 2002, **40**, 1342-1353.
19 H. Xiong, *Solid State Ionics* 2003, **159**, 89-95.
20 B. Hanson, V. Pryamitsyn, V. Ganesan, *ACS Macro Lett.* 2013, **2**, 1001-1005.
21 W. L. Ma, C. Y. Yang, X. Gong, K. Lee, A. J. Heeger, *Adv. Funct. Mater.* 2005, **15**.
22 W. Geens, T. Martens, J. Poortmans, T. Aernouts, J. Manca, L. Lutsen, P. Heremans, S. Borghs, R. Mertens, D. Vanderzande, *Thin Solid Films* 2004, **451-452**, 498-502.
23 N. D. Treat, M. A. Brady, G. Smith, M. F. Toney, E. J. Kramer, C. J. Hawker, M. L. Chabinyc, *Adv. Energy Mater.* 2011, **1**, 82-89.
24 P. Patnaik, *Handbook of Inorganic Chemicals*, McGraw-Hill, 2002.
25 M. Dissanayake, *Ionics* 2004, **10**, 221-225.

26 A. Vallee, S. Besner, J. Prudhomme, *Electrochimica Acta* 1992, *37*, 1579-1583.
27 S. Lascaud, M. Perrier, A. Vallee, S. Besner, J. Prudhomme, M. Armand, *Macromolecules* 1994, **27**, 7469-7477.
28 M. Marzantowicz, J. R. Dygas, F. Krok, A. Lasinska, Z. Florjanczyk, E. Zygadlo-Monikowska, A. Affek, *Electrochimica Acta* 2005, **50**, 3969-3977.
29 M. Marzantowicz, J. R. Dygas, F. Krok, J. L. Nowinski, A. Tomaszewska, Z. Florjanczyk, E. Zygadlo-Monikowska, *J. Power Sources* 2006, **159**, 420-430.
30 D. R. Beech, C. Booth, *J. Polym. Sci. Part B-Polym. Lett.* 1970, **8**, 731.
31 Q. Jiang, C. C. Yang, J. C. Li, *Macromolec. Theo. Sim.* 2003, **12**, 57-60.
32 T. G. Fox, P. J. Flory, *J. Appl. Phys.* 1950, **21**, 581.
33 R. C. Agrawal, G. P. Pandey, *J. Physics D-Appl. Phys.* 2008, *41*.
34 J. R. MacCallum, C.A. Vincent, *Polymer Electrolyte Reviews (v.1)* Springer, 1987.
35 S. Cimmino, R. Greco, E. Martuscelli, L. Nicolais, C. Silvestre, *Polymer* 1978, **19**, 1079-1082.
36 R. F. L. L. E. Nielsen, *Mechanical Properties of Polymers and Composites*, 2nd ed., Marcel Dekker Inc., New York, 1994.
37 S. H. Kim, J. K. Choi, Y. C. Bae, *J. Appl. Polym. Sci.* 2001, **81**, 948-956.
38 R. Mens, S. Chambon, S. Bertho, G. Reggers, B. Ruttens, J. D'Haen, J. Manca, R. Carleer, D. Vanderzande, P. Adriaensens, *Magn. Reson. Chem.* 2011, **49**, 242-247.
39 L. D. Zheng, Y. C. Han, *J. Phys. Chem. B* 2012, **116**, 1598-1604.
40 M. T. Rispens, A. Meetsma, R. Rittberger, C. J. Brabec, N. S. Sariciftci, J. C. Hummelen, *Chem. Commun.* 2003, 2116-2118.
41 M.-S. Hsiao, W. Y. Chen, J. X. Zheng, R. M. Van Horn, R. P. Quirk, D. A. Ivanov, E. L. Thomas, B. Lotz, S. Z. D. Cheng, *Macromolecules* 2008, **41**, 4794-4801.
42 Takahash.Y, H. Tadokoro, *Macromolecules* 1973, **6**, 672-675.
43 L. F. Drummy, R. J. Davis, D. L. Moore, M. Durstock, R. A. Vaia, J. W. P. Hsu, *Chem. Mat.* 2011, **23**, 907-912.
44 J. Chen, X. Yu, K. Hong, J. M. Messman, D. L. Pickel, K. Xiao, M. D. Dadmun, J. W. Mays, A. J. Rondinone, B. G. Sumpter, S. M. Kilbey, II, *J. Mater. Chem.* 2012, **22**, 13013-13022.
45 K. Sivula, Z. T. Ball, N. Watanabe, J. M. J. Frechet, *Adv. Mater.* 2006, **18**, 206.
46 M. C. Stuparu, *Angew. Chem. Int. Ed.* 2013, **52**, 7786-7790.
47 D. Uhrig, J. W. Mays, *J. Polym. Sci. Part A-Polym. Chem.* 2005, **43**, 6179-6222.
48 W. C. Oliver, G. M. Pharr, *J. Mater. Res.* 1992, **7**, 1564-1583.